

Mechanism and energetics of $\langle c + a \rangle$ dislocation cross-slip in hcp metals

Zhaoxuan Wu^{1,2} and W. A. Curtin^{1,*}

¹*Institute of Mechanical Engineering,*

École Polytechnique Fédérale de Lausanne, Lausanne CH-1015, Switzerland

²*Institute of High Performance Computing,*

1 Fusionopolis Way, #16-16 Connexis, Singapore 138632

Abstract

Hexagonal close-packed (hcp) metals such as Mg, Ti, and Zr are lightweight and/or durable metals with critical structural applications in the automotive (Mg), aerospace (Ti), and nuclear (Zr) industries. The hcp structure, however, brings significant complications in the mechanisms of plastic deformation, strengthening, and ductility, and these complications pose significant challenges in advancing the science and engineering of these metals. In hcp metals, generalized plasticity requires the activation of slip on the pyramidal planes, but the structure, motion, and cross-slip of the associated $\langle c + a \rangle$ dislocations are not well established even though they determine ductility and influence strengthening. Here, atomistic simulations in Mg reveal the unusual mechanism of $\langle c + a \rangle$ dislocation cross-slip between pyramidal I and II planes: cross-slip occurs by cross-slip of the individual partial dislocations. The energy barrier is controlled by a fundamental step/jog energy and the near-core energy difference between pyramidal $\langle c + a \rangle$ dislocations. The near-core energy difference can be changed by non-glide stresses, leading to tension-compression asymmetry and even a switch in absolute stability from one glide plane to the other, both features observed experimentally in Mg, Ti and their alloys. The unique cross-slip mechanism is governed by common features of the generalized stacking fault energy surfaces of hcp pyramidal planes and is thus expected to be generic to all hcp metals. An analytical model is developed to predict the cross-slip barrier as a function of the near-core energy difference and applied stresses, and quantifies the controlling features of cross-slip and pyramidal I/II stability across the family of hcp metals.

Keywords: metallurgy — hcp — dislocation — cross-slip — atomistic simulation

* Corresponding author: william.curtin@epfl.ch

Significance

For all hcp metals, the ability to plastically deform in the crystallographic c-axis is crucial for achieving high ductility and high fracture toughness. $\langle c + a \rangle$ dislocation slip is the only sustainable mechanism to accommodate c-axis strain, but has been shown to be difficult across the family of hcp metals. We reveal the mechanism, energy barrier, and unusual stress dependence of $\langle c + a \rangle$ dislocation cross-slip in Mg using atomistic simulations. Our results provide mechanistic insights into $\langle c + a \rangle$ cross-slip behavior, rationalize observed changes in pyramidal I/II slip stability, enable predictions of slip trends across the family of hcp metals, and suggest that applied stresses and/or precise solid solution alloying can optimize cross-slip and enhance c-axis strain capacity, which can ultimately guide design of improved hcp alloys.

Introduction

Plastic deformation of crystalline materials occurs mainly by slip along low-index atomic planes. Slip regions are bounded by line defects called dislocations,¹ which are characterized by the crystallographic slip increment known as the Burgers vector \mathbf{b} and the local line direction $\boldsymbol{\xi}$. The transition from slipped to unslipped regions is resolved at the atomic scale by local atomic rearrangements creating a dislocation “core” structure. Slip occurs by motion of this core, and the surrounding elastic fields, as driven by an applied stress. Plasticity is thus controlled by the details of the core region, which differ significantly among face-centered cubic (fcc), body-centered cubic (bcc), and hexagonal close-packed (hcp) metals.² The motion of the dislocation core is usually confined to glide within the slip plane defined by the normal vector $\mathbf{n} = \mathbf{b} \times \boldsymbol{\xi}$. Screw dislocations have $\mathbf{b} \times \boldsymbol{\xi} = 0$, however, and so do not have a unique slip plane and can therefore “cross-slip” among glide planes that share a common Burgers vector. Cross-slip is a crucial process in plasticity, acting to spread slip spatially on multiple non-parallel planes and to enable dislocation multiplication and annihilation processes; all of these processes affect ductility and ultimate strength of the material. While the atomistic mechanisms, energy barriers and rates of cross-slip are well-established in cubic metals (see Ref.³), the mechanisms in hcp metals are not well-known and are under active study,^{4,5} especially for the technologically important metals Mg, Ti, and Zr.

In hcp metals, only $\langle c + a \rangle$ dislocations, existing on the Pyramidal (Pyr.) I and II planes

(see Fig. 1a), enable plastic slip in the $\langle c \rangle$ direction. The $\langle c + a \rangle$ dislocations are thus essential to achieving generalized plastic flow and, consequently, high ductility and strength. Moreover, experiments demonstrate that the activation of $\langle c + a \rangle$ cross-slip has strong effects on plastic flow evolution and strengthening of hcp metals.^{6–9} Frequent cross-slip of $\langle c + a \rangle$ dislocations can occur in early stage, room temperature deformation.^{9–13} However, the propensity and nature of $\langle c + a \rangle$ cross-slip differ among different materials, and can also depend on the applied stress and temperature in the same material^{10,14–19} (see Fig.2). The range of observed behavior arises in part because, unlike fcc and bcc metals where cross-slip is possible among equivalent slip systems, cross-slip of $\langle c + a \rangle$ dislocations can *only* occur from the structurally different Pyr. I and Pyr. II plane or vice-versa. Although $\langle c + a \rangle$ dislocation core structures are emerging^{20,21} and elastic analyses can help identify which slip system is energetically favorable,^{22,23} there are no studies, criteria, nor mechanisms to rationalize, much less predict, the material, stress, and/or temperature-dependence of cross-slip behavior for the critical $\langle c + a \rangle$ slip in hcp metals.^{2,24}

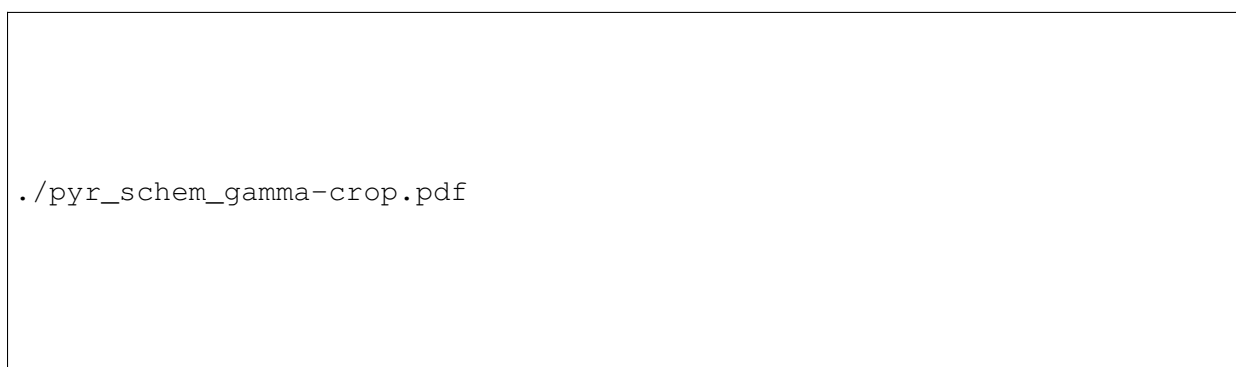


Figure 1. (a) Schematic of the Pyr. I and II planes in the hcp unit cell and the $\langle c + a \rangle$ Burgers vector; (b) and (c) Generalized stacking fault energy surfaces of Pyr. I and II planes, respectively, indicating the Burgers vector, minimum energy path for slip, and energies and positions (“×” symbols) of the metastable stacking faults under full atomic relaxation. The energies are calculated using the MEAM potential for Mg.²⁵

Here, we study the mechanism, energy barrier, and stress dependence of the $\langle c + a \rangle$ screw dislocation cross-slip between Pyr. I and II planes in Mg using the nudged elastic band^{51,52} (NEB) method with a density functional theory (DFT) validated empirical potential.²⁵ We identify a new mechanism of cross-slip, show that the key features enabling this mechanism are common across hcp metals, and develop an analytical model to predict $\langle c + a \rangle$ dislocation cross-slip behavior. The

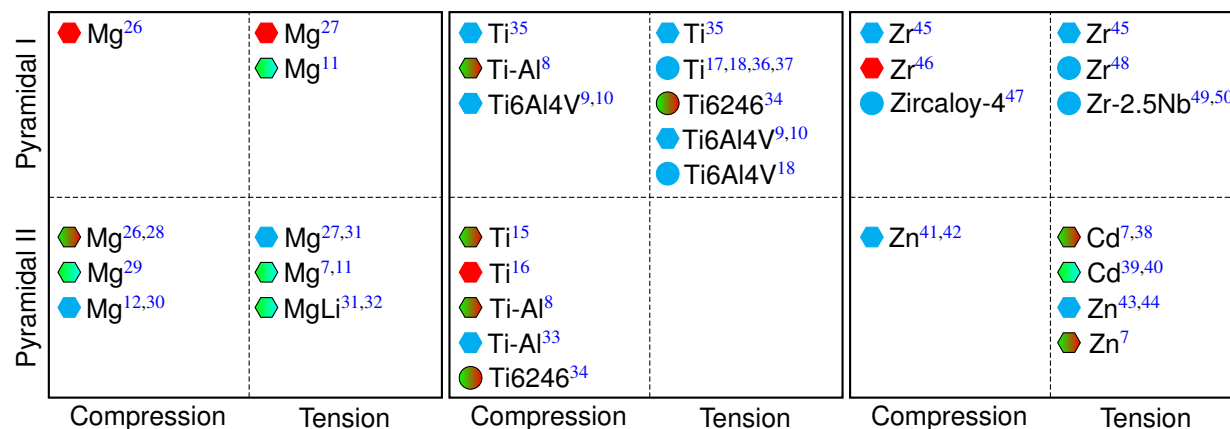


Figure 2. Experimentally observed $\langle c + a \rangle$ dislocation slip planes (Pyr. I and II) for various hcp metals and alloys under a/c-axis compression and tension. In each panel, hexagon and circle symbols represent single and polycrystal tests, respectively, while colors indicate temperature (green = below, blue = at, and red = above room temperature, respectively).

insights and model rationalize the experimentally observed behavior noted above (see also Fig. 2), and provide a framework for design of improved hcp alloys.

Results

In Mg, the $\langle c + a \rangle$ screw dislocations dissociate into a pair of partial dislocations of primarily pure screw character separated by a stacking fault, for both Pyr. I and II planes.^{20,21,25} These dissociations are consistent with the positions of the metastable stacking faults on the generalized stacking fault energy (γ) surfaces⁵³ of the two pyramidal planes as calculated by both DFT^{20,23} and MEAM²⁵ (see Figs. 1 b and c, and SI). The dissociated structure leads to a new cross-slip mechanism, which is revealed by computing the transition pathway for a screw dislocation to move back and forth between Pyr. I and Pyr. II planes. Figure 3a shows the atomic configurations along the minimum energy path (MEP) for cross-slip from Pyr. II onto Pyr. I under stress-free conditions. The cross-slip process has three distinct stages: nucleation, propagation and annihilation. In the first stage, cross-slip is initiated by forming a pair of jogs/steps on *one* of the partial dislocation cores/stacking fault planes. Since the Burgers vectors of the partials are not identical on Pyr. I and II planes, part of the Burgers vector of the migrating partial is also transferred to the other partial through local atom rearrangements. The net effect of this process is the transformation of one

segment of screw dislocation on the Pyr. II plane into a segment on the Pyr. I plane. In the second stage, cross-slip proceeds simply by lateral motion of the jogs/steps along the dislocation line, thus shifting more segments onto the Pyr. I plane. In the third stage, the left and right jogs/steps become sufficiently close that they begin to annihilate. For cross-slip from Pyr. I onto Pyr. II, the path is reversed so that the third stage shown in Fig. 3a is the nucleation stage. The unique constriction-free $\langle c + a \rangle$ dislocation cross-slip mechanism shown in Mg is the first main result of this paper.

Unlike dislocations in fcc and bcc metals, the $\langle c + a \rangle$ dislocations on the initial and final slip planes have different core structures, stacking faults, relative partial orientation and, therefore, different near-core energies per unit length E_{struc} . The far-field elastic energies are the same.^{1,23,55} Cross-slip between Pyr. I and II planes thus leads to a net change in total dislocation energy, which influences the cross-slip energy barrier. For Mg, our simulations show that the $\langle c + a \rangle$ screw dislocation has a lower energy on the Pyr. II plane as compared to the Pyr. I plane. The energy difference is small, ~ 30 meV/nm, but has a crucial effect on cross-slip: the energy barrier for cross-slip of a dislocation segment depends on the segment length. To illustrate this feature, we perform NEB calculations for 3 different dislocation lengths ($l=146, 219, 292$ Å) under stress-free conditions. Figure 3b shows the atomic configurations along the MEP for a longer length, demonstrating that the underlying three-stage process is length-independent. However, the energies along the MEP are length-dependent, as shown in Figs. 3c and d. In Fig. 3c, the energy difference is shown relative to the low-energy Pyr. II screw, while Fig. 3d shows the energy difference relative to the higher energy Pyr. I screw. The reaction coordinate of replica j is the accumulated distance (in Å) along the path in terms of the replica coordinate \mathbf{x} , i.e., $d_j = \sum_{i=1}^j \sqrt{(\mathbf{x}_i - \mathbf{x}_{i-1}) \cdot (\mathbf{x}_i - \mathbf{x}_{i-1})}$. In Stage 1 (nucleation, $0 < d < 17$), there is a sharp rise in energy that is similar for all three lengths (Fig. 3c). During Stage 2 (propagation, $17 < d < d_{\text{max}} - 12$), the energy difference increases linearly with increasing d , due purely to the difference in Pyr. I and Pyr. II dislocation near-core energies. The extent of the linear region, and the associated increase in energy barrier, scales directly with the dislocation length l . In Stage 3 (annihilation, $d_{\text{max}} - 12 < d < d_{\text{max}}$ but also the nucleation stage starting from the Pyr. I screw), the energy decreases to the total energy of the straight Pyr. I dislocation, and is the same for all three lengths (see Fig. 3d). The cross-slip energy barrier $\Delta G_{\text{II-I}}$ for slip from Pyr. II to Pyr. I is thus dependent on the total length of cross-slipping segment, while the barrier for the reverse process $\Delta G_{\text{I-II}}$, from Pyr. I to Pyr. II, is independent of length and much smaller.

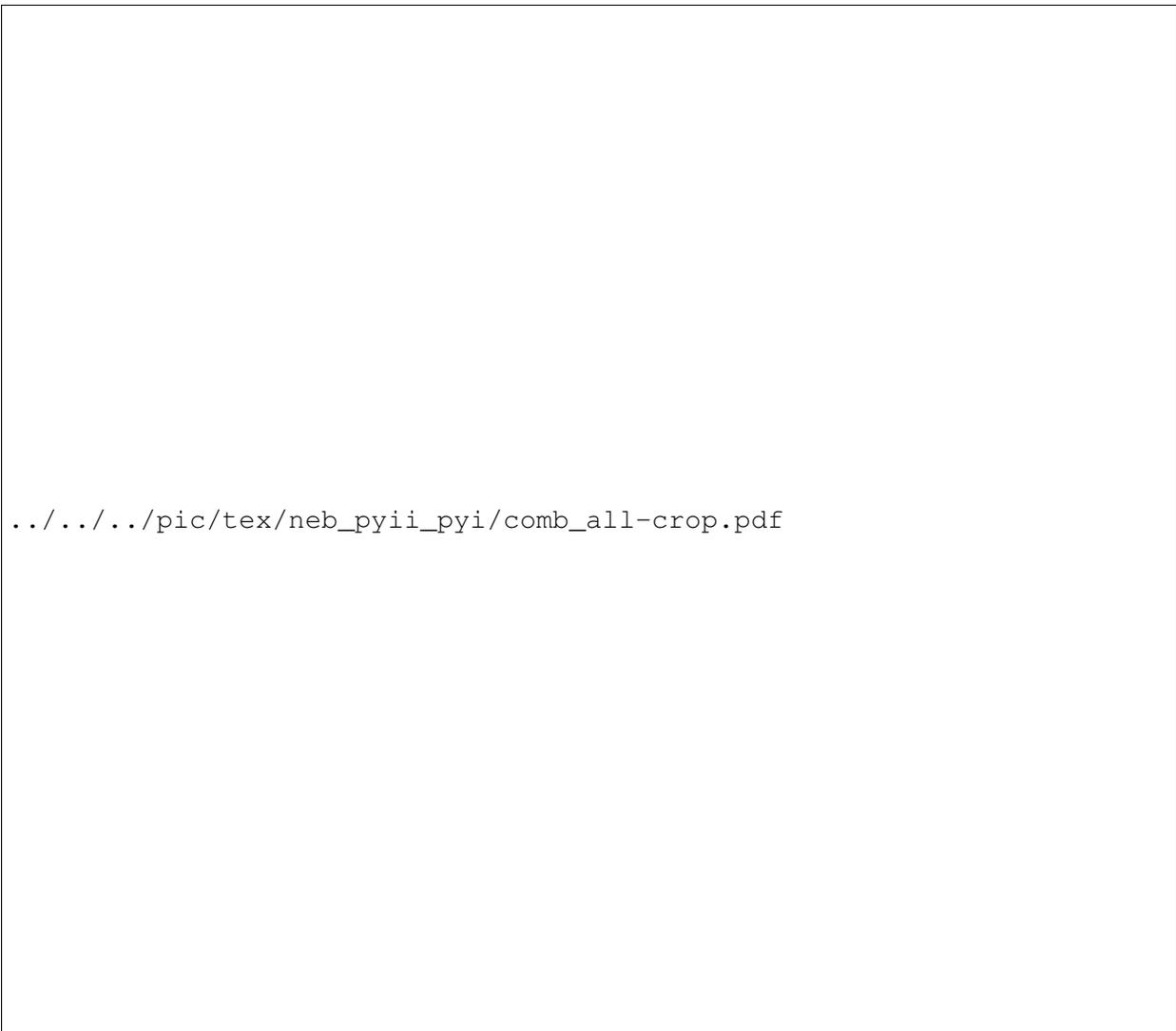


Figure 3. Atomic configurations and energy profiles along the minimum energy path (MEP) for $\langle c + a \rangle$ screw dislocation cross-slip from Pyr. II to I planes (left to right), as calculated by NEB under stress-free conditions. (a) dislocation length $l = 146 \text{ \AA}$; (b) dislocation length $l = 292 \text{ \AA}$. On top of each image, the number indicates the corresponding reaction coordinate d shown in (c) and (d); (c) Energy versus path coordinate for $\langle c + a \rangle$ screw dislocations at three different lengths cross-slip, with reference to the lower-core-energy Pyr. II dislocation; (d) as in (c) but with reference to the higher-core-energy Pyr. I dislocation. In (c) and (d), the energy barrier for cross-slip from the Pyr. II to the Pyr. I plane is denoted as $\Delta G_{\text{II-I}}$ and depends on dislocation length, while that for cross-slip from Pyr. I to Pyr. II is denoted $\Delta G_{\text{I-II}}$ and is length-independent. Atoms are colored on the basis of common neighbor analysis:⁵⁴ purple = bcc; yellow = others. Dislocation cores are shown with only non-hcp atoms.

Therefore, under stress-free conditions, a typical long Pyr. II screw dislocation ($l > 20$ nm) is highly unlikely to cross-slip entirely onto the Pyr. I plane because of the very high barrier ($\Delta G_{II-I} > 0.8$ eV), while a Pyr. I screw dislocation of any length will cross-slip rapidly (~ 1 ns at room temperature) over the low barrier ($\Delta G_{I-II} \sim 0.24$ eV) onto the Pyr. II plane. Note that room-temperature MD simulations using short dislocation lengths ($l < 5$ nm) show frequent cross-slip that is not pertinent to real behavior. We conclude that at *low* stresses and *low* temperatures, $\langle c + a \rangle$ slip on Pyr. II planes is expected to be dominant in Mg, consistent with data in Fig. 2, and with past^{26,28} and very recent^{12,30} TEM studies reporting (sessile) dislocations primarily aligned with the $[\bar{1}010]$ direction that can come only from Pyr. II $\langle c + a \rangle$ slip. The general control and asymmetry of Pyr. I/II cross-slip energy barriers caused by the near-core energy difference, and the specific preference for Pyr. II slip in Mg, constitute the second main result of this paper.

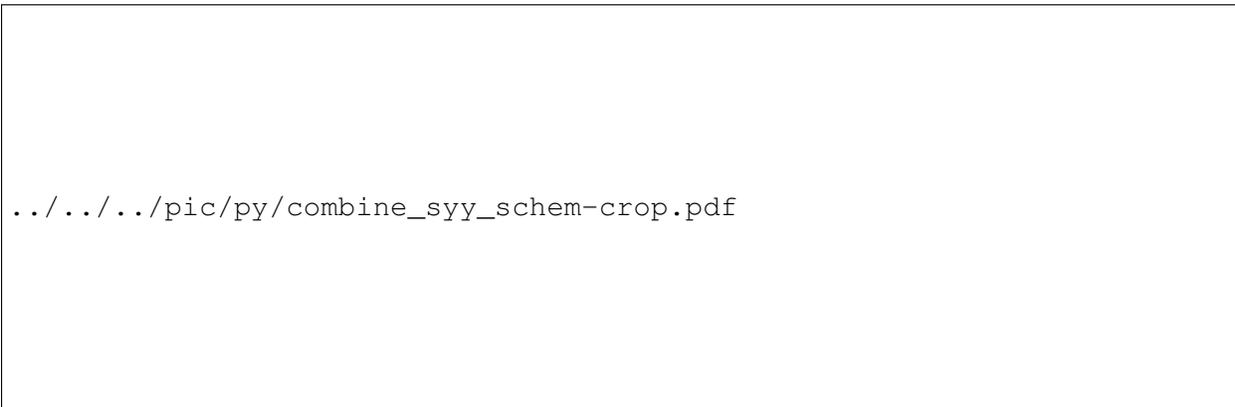


Figure 4. (a) Dislocation energy differences $E_I - E_{II}$ as a function of applied normal stress σ_{yy} . (b,c) Energy profiles on the minimum energy path for $\langle c + a \rangle$ screw dislocation cross-slip from Pyr. II to I planes calculated by NEB under applied normal stress σ_{yy} .

The near-core energy difference per unit length ($E_I - E_{II}$) between Pyr. II and I dislocations can, however, be changed by applied non-glide stresses through interactions with the dislocation cores and stacking faults, with a possible Escaig-stress effect⁵⁶ on the small edge components of the Pyr. I partials. Figure 4a shows the energy difference $E_I - E_{II}$ as a function of applied stress σ_{yy} normal to the Pyr. II plane. The stress σ_{yy} is related to the standard single crystal a/c -axis loading directions via a geometrical factor as indicated in Fig. 4a. Compressive stresses *increase* the energy difference, making Pyr. II even more favorable, while tensile stresses on the Pyr. II plane *decrease* the energy difference, making Pyr. I less unfavorable. In fact, at high tensile stresses (> 660 MPa), absolute stability of the $\langle c + a \rangle$ dislocation changes: the $\langle c + a \rangle$ screw

dislocation has a lower energy on the Pyr. I plane. Related effects are seen for other stress states (see SI and Fig. S3). The cross-slip energy barrier then also depends on these applied stresses. Figures 4 b and c show the energy along the MEP at one length ($l = 292 \text{ \AA}$) for $\langle c + a \rangle$ screw dislocation cross-slip under applied stresses σ_{yy} . Consistent with the absolute changes in relative near-core energy, compressive stresses increase $\Delta G_{\text{II-I}}$ while tensile stresses decrease it. The change in $\Delta G_{\text{II-I}}$ is mainly manifested in changes in the slope in Stage 2. The applied stress gives a similar trend for the energy barrier in Stage 1 (nucleation process). Thus, tensile stresses on the Pyr. II plane also lower the energy barrier for forming a segment of dislocation on the Pyr. I plane. In contrast, σ_{yy} has little effect on $\Delta G_{\text{I-II}}$. Therefore, tensile σ_{yy} increases the net rate of cross-slip onto Pyr. I while not affecting the rate of the reverse process. This normal-stress dependence of the near-core energy difference and its influence on cross-slip is the third main result of this paper.

Our atomistic analyses were executed on Mg, due to the existence of a well-validated inter-atomic potential. But the observed phenomena and mechanisms are expected to be common to hcp metals. Firstly, for hcp Mg, Ti, Zr, Co, Cd, and Zn, both the Pyr. I and Pyr. II γ -surfaces show the existence of metastable fault vectors generally aligned with the $\langle c + a \rangle$ Burgers vector⁵⁷⁻⁵⁹ (see Fig. S2 and SI). These fault vectors are largely dictated by crystal symmetries. Pyr. I and Pyr. II near-core energies are also generally different, so that the asymmetry in cross-slip is also expected. Finally, experimental observations indicated that relative stability between Pyr. I and II can change with loading (see Fig. 2), consistent with a dependence of near-core energies on non-glide stresses.

In spite of the difficulty of cross-slip under zero glide stress, cross-slip can be facilitated by resolved shear glide stresses on the cross-slip plane. So, when a dislocation on the primary slip plane is pinned by other metallurgical features (precipitates, solutes, forest dislocations) such that local screw segments on the primary plane experience resolved shear stress below their Peierls stresses, resolved shear stresses above the Peierls stress can still exist on the cross-slip plane. This shear stress provides a driving force that reduces the energy barrier for cross-slip. Incorporating all mechanistic factors, we can develop a general analytical model for pyramidal dislocation cross-slip in hcp materials as follows. Because the Pyr. I and II dislocations glide readily at low applied stresses at room temperature, we use a line-tension framework and study a configuration with a cross-slipped segment bowing out on the cross-slip plane, as shown in Fig. 5a (see SI). For cross-slip between two structurally different planes, the cross-slip energy barrier has a number of

contributions,³

$$\Delta G = E_s + \Delta E(\boldsymbol{\sigma})l + T\Delta s(T, b, \tau, l) - \tau bA(T, b, \tau, l) \quad (1)$$

where E_s is the intrinsic energy associated with the jogs/steps connecting the cross-slipped and uncross-slipped dislocation segments (corresponding to stage 1 or stage 3), $\Delta E(\boldsymbol{\sigma})$ is the stress-dependent near-core energy difference between the two glide planes, l is the chord length of the putative cross-slipped dislocation, T is the line tension, Δs is the additional dislocation line length due to bow-out, τ is the resolved shear stress on the cross-slip plane, and A is the area swept by the dislocation during the bow-out. Crucially, the work done by the applied stress, the last term in Eqn. 1, can overcome the length-dependent near-core energy difference that prohibits cross-slip at zero stress.

At stress τ , the cross-slipped segment can expand unbounded if it can reach a critical length l_c determined by $\partial\Delta G/\partial l = 0$. Approximating the bow out geometry as circular arc with arc length s and area A (see SI) gives l_c as

$$l_c = \frac{2\sqrt{\Delta E(\boldsymbol{\sigma})(2T - \Delta E(\boldsymbol{\sigma}))}}{b\tau}. \quad (2)$$

Inserting l_c into Eqn. 1 yields the activation barrier for nucleating onto the cross-slip plane. The result is not analytic and so we show a numerical example below. In general, however, increasing the shear stress on the cross-slip plane makes both the critical length l_c and the activation energy barrier smaller, increasing the rate of thermally-activated cross-slip.

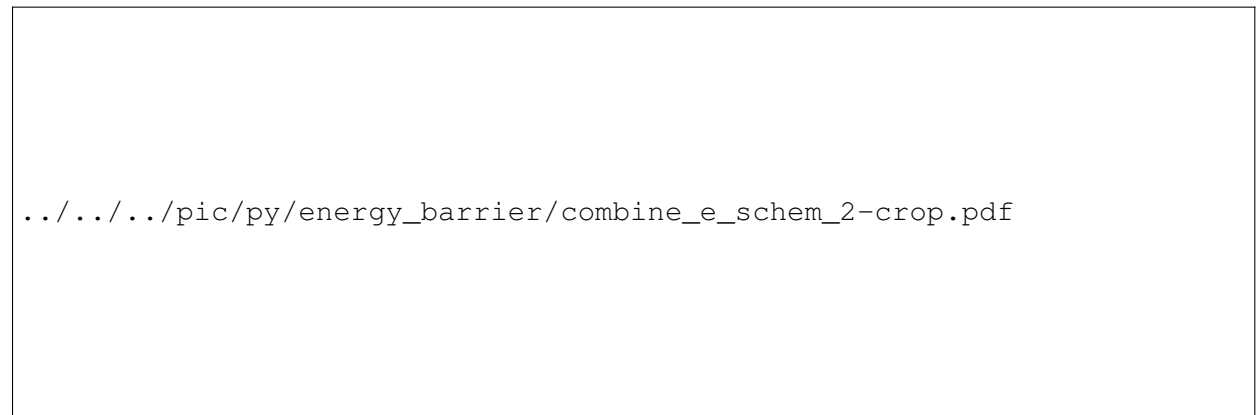


Figure 5. (a) Schematic of dislocation cross-slip configuration. (b) Cross-slip energy barrier ΔG as a function of cross-slip length l under resolved shear stress τ on cross-slip plane. (c) Cross-slip energy barrier ΔG as a function of resolved shear stress τ and normal stress σ_{yy} .

As a concrete example relevant to Mg, we use atomistically-derived values $E_s = 0.23$ eV and $\Delta E(\sigma)$ (Fig. 4a), and approximate $T = 0.5\mu b^2$ where μ is the shear modulus. The cross-slip energy barrier ΔG as a function of l versus applied shear stress τ is shown in Figures 5b; the critical length l_c and energy barrier correspond to the maximum value of ΔG at each stress value. The barrier cannot decrease below E_s , but even at moderate stresses (~ 80 MPa), the barrier is not significantly higher (~ 0.35 eV) and at an accessible nanoscale length ($l_c \approx 7$ nm). Thus, cross-slip from Pyr. II to Pyr. I can become quite frequent under conditions typical of Mg processing and/or applications. Easy cross-slip thus also makes it difficult to experimentally determine the primary/dominant slip plane.¹³

Moreover, Figure 5c shows the activation energy versus resolved shear stress τ for a range of applied non-glide normal stresses σ_{yy} , using Mg values. For all τ , tensile σ_{yy} reduces the energy barrier for cross-slip while compressive σ_{yy} increases the energy barrier. This is consistent with experimental observations where Pyr. II slip is commonly seen in c-axis compressive loading^{12,26,28} but where Pyr. I slip becomes more important/frequent at high temperatures or in tensile loading^{26,27} (see Fig. 2). At $\tau = 50$ MPa and σ_{yy} within ± 100 MPa (typical values at the onset of yield at room temperature in single crystal Mg under a/c-axis deformation⁷), we find ΔG is $\sim 0.42 \pm 0.04$ eV. At laboratory strain rates, cross-slip is thus predicted to be particularly active at room temperature but unlikely at 77 K. However, the Pyr. I screw $\langle c + a \rangle$ can only glide for a short distance before cross-slipping back to the Pyr. II planes. Thus, frequent double cross-slip is expected, consistent with various experiments^{7,12,31,32} with Pyr. II $\langle c + a \rangle$ slip dominant. At the same time, under c-axis compression loading at room temperature, single crystal Mg strain-hardens rapidly^{12,13,28,60} with the flow stress reaching ~ 300 MPa within a few percent strain. The increase in flow stress increases τ and σ_{yy} proportionally (see Fig. 4), so that the net effect, per results in Fig. 5c, is to decrease the cross-slip energy barrier and increase the dislocation cross-slip rate. This enables more Pyr. I slip at later stages of deformation. At even higher stresses, such as those during cold rolling of polycrystals,⁶¹ $\langle c + a \rangle$ screw dislocations in some grains may have similar energies on Pyr. I and Pyr. II so that $\Delta E = 0$ (see SI). Then, the barriers for cross-slip from Pyr. I to II planes and vice versa may become comparable, making $\langle c + a \rangle$ slip equally favorable on Pyr. I and II planes. The above conclusions are all in general agreement with experiments on Mg where deformation mechanisms are most clearly discernable, and rationalize the experimental ambiguities^{13,61–63} in the competition between Pyr. II and Pyr. I slips in Mg.

Looking more generally across the family of hcp metals shown in Fig. 2, differences among

them arise due to differences in Pyr. I and Pyr. II stacking fault, core, and jog/step energies, and their dependencies on non-glide stresses. For Ti, $\langle c + a \rangle$ slip on Pyr. I is more common, indicating that the Pyr. I screw has lower energy than the Pyr. II screw; this is consistent with our DFT calculations showing the metastable stacking fault energy on Pyr. I to be less than half of that on Pyr. II planes. However, $\langle c + a \rangle$ cross-slip is frequently observed in Ti and Ti alloys at high temperatures or under a/c-axis compressive loadings (see Fig. 2); this indicates that both the energy difference $E_I - E_{II}$ and the cross-slip activation energy barrier ΔG_{I-II} are relatively low in Ti and can be modified by stresses in the same way as found here for Mg. Furthermore, the high flow stresses in Ti alloys may also help reduce the cross-slip activation energy barrier for cross-slip onto Pyr. II planes. In fact, new experiments, using micro-cantilever bending⁹ to induce both tension and compression in the same sample under the same conditions, clearly show Pyr. I slip in tension but wavy Pyr. I+II slip in compression. In contrast to Mg and Ti, $\langle c + a \rangle$ cross-slip is not common in hcp metals like Zn, Cd and Zr, nor is there evidence of any switch in dominant slip system between Pyr. I and Pyr. II (see Fig. 2). This indicates that the difference in Pyr. I and II dislocation near-core energies and/or the step/jog energy are relatively larger in Zn, Cd, and Zr, and thus with larger energy barriers, but the mechanisms should remain the same since their γ -surface profiles are similar to those of Mg and Ti (see SI).

Our analysis shows that the cross-slip frequency and relative stability depend on the near-core energy difference between Pyr. I and II screw dislocations. This suggests that alloying with solutes, which interact with the dislocation cores and stacking faults, can shift the near-core energy difference and, therefore, shift the relative stability of Pyr. I and II and change the frequency of cross-slip. Indeed, experiments show that the dominant slip system (and thus the cross slip) is influenced by alloying in Mg and Ti (see Fig. 2). This further suggests that precise solid solution alloying could maximize/optimize cross-slip in Mg and Ti to achieve a desired evolution of plasticity. Of course, such alloying will have many other effects such as strengthening of all the various hcp slip systems, so that optimization is multi-dimensional. For Mg, with other strategies aimed at enhancing c-axis strain capacity under active research⁶¹ and some apparently exhausted,^{55,64} optimizing cross-slip may provide fresh opportunities. In contrast, since Zr, Zn, and Cd likely have larger near-core energy differences between Pyr. I and II screw cores, leading to high dominance of one of the two pyramidal slip systems, solid solution alloying would be less likely to alter the dominant slip system. But alloying could still significantly influence the rate of double cross-slip. There are relatively fewer direct observations in Zn^{41,42} and Cd,^{7,38} so future

experiments and simulations would provide further insights.

In summary, the crystallographic features of hcp pyramidal planes drive $\langle c + a \rangle$ screw dislocation dissociation into near-screw partials, which allows for a new mechanism of cross slip. However, the screw dislocations on Pyr. I and II have different energies, greatly affecting the cross-slip barriers and rates. This energy difference also depends on non-glide stresses, leading to tension/compression asymmetry in cross-slip and slip plane dominance. These new insights rationalize a wide body of experimental literature in hcp metals and provide a mechanistic basis for modifying $\langle c + a \rangle$ slip via targeted alloying, for instance. The unusual features of hcp pyramidal cross-slip must also be incorporated into higher-scale modelings such as dislocation dynamics and crystal plasticity models, if such models are to accurately reflect real plasticity mechanisms in hcp metals. The work here provides quantitative results for Mg, which can be made even more quantitative with additional first-principles studies, and provides a firm basis for future quantitative work on Ti, Zr, and other hcp metals. Combined with other recent works,^{55,57,65,66} computational metallurgy is now revealing the rich, distinct, and complex behavior in a class of materials, hcp metals, that have high technological value.

Methods

Atomistic simulations and NEB calculations are performed using LAMMPS⁶⁷ with Mg atom interactions described by a modified embedded-atom method^{68,69} potential parametrized by Wu *et al.*²⁵ In the current NEB calculations, 64, 96, 128 replicas are used for dislocation of lengths 146, 219, 292 Å. Unless otherwise stated, convergence is assumed when the maximum force on atoms is below 10^{-4} eVÅ⁻¹. More details on the simulation cell and boundary conditions are described in the SI.

Acknowledgments

Z.W. acknowledges the financial support from the Agency for Science, Technology and Research (A*STAR), Singapore. W.A.C. acknowledges support of this work through a European Research Council Advanced Grant, “Predictive Computational Metallurgy”, ERC Grant agreement No. 339081 - PreCoMet. Part of the computer time was supported by a grant from the Swiss

National Supercomputing Centre (CSCS) under project ID s631.

- [1] J. P. Hirth and J. Lothe, *Theory of Dislocations*, 2nd ed. (John Wiley & Sons, 1982).
- [2] V. Vitek and V. Paidar, in *Dislocations in Solids*, Vol. 14, edited by J. P. Hirth (Elsevier, 2008) Chap. 87, pp. 439–514.
- [3] W. Püschl, *Progress in Materials Science* **47**, 415 (2002).
- [4] J. A. Yasi, L. G. Hector Jr., and D. R. Trinkle, *Acta Materialia* **59**, 5652 (2011).
- [5] J. A. Yasi, L. G. Hector Jr., and D. R. Trinkle, *Acta Materialia* **60**, 2350 (2012).
- [6] M. A. W. Lowden and W. B. Hutchinson, *Metallurgical Transactions A* **6**, 441 (1975).
- [7] H. Tonda and S. Ando, *Metallurgical and Materials Transactions A - Physical Metallurgy and Materials Science* **33**, 831 (2002).
- [8] J. C. Williams, R. G. Baggerly, and N. E. Paton, *Metallurgical and Materials Transactions A - Physical Metallurgy and Materials Science* **33**, 837 (2002).
- [9] R. Ding, J. Gong, A. J. Wilkinson, and I. P. Jones, *Acta Materialia* **76**, 127 (2014).
- [10] I. P. Jones and W. B. Hutchinson, *Acta Metallurgica* **29**, 951 (1981).
- [11] S. Ando, K. Nakamura, K. Takashima, and H. Tonda, *Journal of Japan Institute of Light Metals* **42**, 765 (1992).
- [12] J. Geng, M. F. Chisholm, R. K. Mishra, and K. S. Kumar, *Philosophical Magazine*, *Philosophical Magazine* **95**, 3910 (2015).
- [13] K. Y. Xie, Z. Alam, A. Caffee, and K. J. Hemker, *Scripta Materialia* **112**, 75 (2016).
- [14] M. H. Yoo and C. T. Wei, *Journal of Applied Physics* **38**, 4317 (1967).
- [15] Y. Minonishi, S. Morozumi, and H. Yoshinaga, *Scripta Metallurgica* **16**, 427 (1982).
- [16] Y. Minonishi, S. Morozumi, and H. Yoshinaga, *Scripta Metallurgica* **19**, 1241 (1985).
- [17] H. Numakura, Y. Minonishi, and M. Koiwa, *Scripta Metallurgica* **20**, 1581 (1986).
- [18] S. Zaeferrer, *Materials Science and Engineering: A* **344**, 20 (2003).
- [19] B. Barkia, V. Doquet, J. P. Couzinié, I. Guillot, and E. Hériprié, *Materials Science and Engineering: A* **636**, 91 (2015).
- [20] M. Ghazisaeidi, L. G. Hector Jr, and W. A. Curtin, *Scripta Materialia* **75**, 42 (2014).
- [21] M. Itakura, H. Kaburaki, M. Yamaguchi, and T. Tsuru, *Physical Review Letters* **116**, 225501 (2016).
- [22] P. B. Legrand, *Philosophical Magazine Part B* **49**, 171 (1984).

- [23] Z. Wu, B. Yin, and W. A. Curtin, *Acta Materialia* **119**, 203 (2016).
- [24] S. R. Agnew, “Deformation mechanisms of magnesium alloys,” in *Advances in Wrought Magnesium Alloys: Fundamentals of Processing, Properties and Applications* (Woodhead Publishing Limited, 2012) Chap. 2, pp. 63–104.
- [25] Z. Wu, M. F. Francis, and W. A. Curtin, *Modelling and Simulation in Materials Science and Engineering* **23**, 015004 (2015).
- [26] J. F. Stohr and J. P. Poirier, *Philosophical Magazine* **25**, 1313 (1972).
- [27] S. Ando, A. Kodera, K. Fukushima, M. Tsushida, and H. Kitahara, *Materials Science Forum* **783-786**, 341 (2014).
- [28] T. Obara, H. Yoshinga, and S. Morozumi, *Acta Metallurgica* **21**, 845 (1973).
- [29] T. Kitahara, S. Ando, M. Tsushida, H. Kitahara, and H. Tonda, *Key Engineering Materials* **345-346**, 129 (2007).
- [30] J. Geng, M. F. Chisholm, R. K. Mishra, and K. S. Kumar, *Philosophical Magazine Letters* **94**, 377 (2014).
- [31] S. Ando and H. Tonda, *Materials Science Forum* **350-351**, 43 (2000).
- [32] S. Ando and H. Tonda, *Materials Transactions* **41**, 1188 (2000).
- [33] J. Kwon, M. C. Brandes, P. Sudharshan Phani, A. P. Pilchak, Y. F. Gao, E. P. George, G. M. Pharr, and M. J. Mills, *Acta Materialia* **61**, 4743 (2013).
- [34] X. Feaugas and M. Clavel, *Acta Materialia* **45**, 2685 (1997).
- [35] J. Gong and A. J. Wilkinson, *Acta Materialia* **57**, 5693 (2009).
- [36] A. A. Pochettino, N. Gannio, C. V. Edwards, and R. Penelle, *Scripta Metallurgica et Materialia* **27**, 1859 (1992).
- [37] L. Wang, R. Barabash, T. Bieler, W. Liu, and P. Eisenlohr, *Metallurgical and Materials Transactions A-Physical Metallurgy and Materials Science* **44**, 3664 (2013).
- [38] J. Krásová and P. Kratochvíl, *Physica Status Solidi (a)* **7**, 255 (1971).
- [39] P. B. Price, *Journal of Applied Physics* **32**, 1750 (1961).
- [40] H. Tonda, S. Ando, K. Takashima, and T. Vreeland Jr., *Acta Metallurgica et Materialia* **42**, 2845 (1994).
- [41] K. H. Adams, R. C. Blish, and T. Vreeland Jr., *Materials Science and Engineering* **2**, 201 (1967).
- [42] R. C. Blish II and T. Vreeland Jr., *Journal of Applied Physics* **40**, 884 (1969).

- [43] R. L. Bell and R. W. Cahn, Proceedings of the Royal Society of London A: Mathematical, Physical and Engineering Sciences **239**, 494 (1957).
- [44] P. B. Price, Philosophical Magazine **5**, 873 (1960).
- [45] J. Gong, T. Benjamin Britton, M. A. Cuddihy, F. P. E. Dunne, and A. J. Wilkinson, Acta Materialia **96**, 249 (2015).
- [46] A. Akhtar, Journal of Nuclear Materials **47**, 79 (1973).
- [47] P. Merle, Journal of Nuclear Materials **144**, 275 (1987).
- [48] H. Numakura, Y. Minonishi, and M. Koiwa, Philosophical Magazine A **63**, 1077 (1991).
- [49] F. Long, M. R. Daymond, and Z. Yao, Journal of Applied Physics **117**, 094307 (2015).
- [50] F. Long, M. R. Daymond, Z. Yao, and M. A. Kirk, Journal of Applied Physics **117**, 104302 (2015).
- [51] G. Henkelman and H. Jónsson, Journal of Chemical Physics **113**, 9978 (2000).
- [52] G. Henkelman, B. P. Uberuaga, and H. Jónsson, Journal of Chemical Physics **113**, 9901 (2000).
- [53] V. Vitek, Philosophical Magazine **18**, 773 (1968).
- [54] D. Faken and H. Jónsson, Computational Materials Science **2**, 279 (1994).
- [55] Z. Wu and W. A. Curtin, Nature **526**, 62 (2015).
- [56] B. Escaig, Journal de Physique **29**, 225 (1968).
- [57] M. Ghazisaeidi and D. R. Trinkle, Acta Materialia **60**, 1287 (2012).
- [58] E. Clouet, Physical Review B **86**, 144104 (2012).
- [59] N. Chaari, E. Clouet, and D. Rodney, Metallurgical and Materials Transactions A **45**, 5898 (2014).
- [60] C. M. Byer, B. Li, B. Cao, and K. T. Ramesh, Scripta Materialia **62**, 536 (2010).
- [61] S. Sandlöbes, M. Friák, J. Neugebauer, and D. Raabe, Materials Science and Engineering: A **576**, 61 (2013).
- [62] S. R. Agnew, D. W. Brown, and C. N. Tomé, Acta Materialia **54**, 4841 (2006).
- [63] H. Fan and J. A. El-Awady, Materials Science and Engineering: A **644**, 318 (2015).
- [64] Z. Wu and W. A. Curtin, Scripta Materialia **116**, 104 (2016).
- [65] N. Chaari, E. Clouet, and D. Rodney, Physical Review Letters **112**, 075504 (2014).
- [66] E. Clouet, D. Caillard, N. Chaari, F. Onimus, and D. Rodney, Nature Materials **14**, 931 (2015).
- [67] S. Plimpton, Journal of Computational Physics **117**, 1 (1995).
- [68] M. I. Baskes, Physical Review B **46**, 2727 (1992).
- [69] B.-J. Lee and M. I. Baskes, Physical Review B **62**, 8564 (2000).

- [70] R. G. Hennig, T. J. Lenosky, D. R. Trinkle, S. P. Rudin, and J. W. Wilkins, *Physical Review B* **78**, 054121 (2008).
- [71] M. I. Mendeleev and G. J. Ackland, *Philosophical Magazine Letters* **87**, 349 (2007).
- [72] G. P. P. Pun and Y. Mishin, *Physical Review B* **86**, 134116 (2012).
- [73] X. W. Zhou, M. E. Foster, F. B. van Swol, J. E. Martin, and B. M. Wong, *The Journal of Physical Chemistry C* **118**, 20661 (2014).
- [74] D. K. Ward, X. Zhou, B. M. Wong, and F. P. Doty, *Journal of Molecular Modeling* **19**, 5469 (2013).

Supporting Information

Simulation cells and boundary conditions

In anisotropic linear elastic medium, the displacement field \mathbf{u} of a straight Volterra dislocation with Burgers vector \mathbf{b} can be obtained using the Stroh formalism.^{1,23} The Volterra solution \mathbf{u} is completely determined by the Burgers vector and the elastic stiffness tensor of the material, independent of the dislocation core relaxation or dissociations. For a dislocation in real materials, the displacement field \mathbf{u} near the core region is further modified due to core dissociation and relaxation beyond linear elasticity, while in the far field, the Volterra solution is accurate. In atomistic simulations of finite sizes, to simulate an isolated dislocation in an infinite elastic medium, all atoms are first displaced according to the Volterra solution \mathbf{u} , followed by a relaxation process where atoms within $2 \times$ the cut off distance ($2r_c$, see Fig. S1) from the outer boundary are fixed in positions, while atoms inside are relaxed according to their atomistic forces as prescribed by the interatomic potential. To simulate an isolated dislocation in stressed elastic medium, the same displace-relax procedure is used, but with the initial displacement field replaced by the superposition of the displacement field corresponding to the desired stress and the Volterra displacement field.

For each NEB simulation in this work, we start with a base simulation cell of perfect hcp lattice created with x in the $[10\bar{1}0]$ direction, y normal to the Pyr. II plane and z in the $[11\bar{2}3]$ direction. The base simulation cell has dimensions ($l_x \times l_y \times l_z$) of $\sim 100 \text{ nm} \times 100 \text{ nm} \times 2 \text{ nm}$. A straight $\langle \mathbf{c} + \mathbf{a} \rangle$ Pyr. II screw dislocation along the periodic z -axis is created and relaxed at the center of the base cell following the above displace-relax procedure. Simulation cells with a Pyr. I screw dislocation is obtained by applying a tensile stress of 750 MPa normal to the Pyr. II plane and running molecular dynamics at 77 K. Under these simulation conditions, the screw $\langle \mathbf{c} + \mathbf{a} \rangle$ dissociated on the Pyr. II plane transforms into a screw $\langle \mathbf{c} + \mathbf{a} \rangle$ dissociated on the Pyr. I plane. The Pyr. I core thus obtained is further relaxed using the same boundary conditions of the previous Pyr. II core. The NEB cells ($\sim 20 \text{ nm} \times 20 \text{ nm} \times 2 \text{ nm}$), shown in Figs. S1 a and b, are cut from the base cells with the dislocation dissociated on the Pyr. II or Pyr. I plane, thus forming the start and end replicas in the NEB calculations. In each NEB cell, atoms within $2r_c$ from the outer boundary are treated as boundary atoms. Their positions, taken from the start replica, are thus fixed and used

as boundary conditions for all replicas in subsequent NEB calculations. Dislocations of different lengths are created by replicating the cell in the z -direction.

Pyramidal γ -surface of hcp metals

The γ -surfaces of Pyr. I and II planes are calculated for a total of six hcp metals using available interatomic potentials, as shown in Fig. S2. The positions and energies of metastable stacking faults are obtained under full atomic relaxation. Among all the cases, the minimum energy path and the position of metastable stacking faults are similar. Therefore, in these metals $\langle c + a \rangle$ dislocation dissociations on Pyr. I and II planes are expected to be similar to that shown for Mg. We note that these interatomic potentials use various different formalisms (MEAM, EAM, Bond-order), yet they exhibit similar features in the calculated γ -surface profiles. In addition, DFT calculations²³ show qualitatively similar results. All these suggest the general features of the γ -surface are strongly dictated by crystal symmetry while the details of atomic bonding influence the fine positions and energetics of these features.

Effect of non-Schmid stresses on dislocation energy and cross-slip barriers

The effects of non-Schmid stresses σ_{xx} and σ_{xy} on dislocation energy and cross-slip barriers are calculated and shown in Fig. S3. Tensile σ_{xx} increases the energy difference, making Pyr. II more favorable relative to Pyr. I; compressive σ_{xx} has an opposite effect. In terms of tension v.s. compression, the effects of σ_{xx} is opposite to that of σ_{yy} , as expected. In contrast, σ_{xy} decreases the energy difference and makes cross-slip easier, independent of the direction of shear. At $\sigma_{xy} \approx \pm 250$ MPa, Pyr. I and II planes are equally favorable and the activation energies for cross-slip from Pyr I to II and vice versa are the same and equal to the jog/step energy, ~ 0.23 eV (see Fig. S3). Slip can thus occur on both planes and cross-slips are expected to be very active at temperatures higher than 77 K. The relative slip activities between Pyr. I and II planes then depend on the Schmid stresses and the mobilities of the $\langle c + a \rangle$ dislocations on these two planes. In addition, a metastable structure is found at $\sigma_{xx} = 250$ MPa and $\sigma_{xy} = \pm 125$ MPa. This metastable structure reduces the activation energy barrier for cross-slip from Pyr. I to II planes to ~ 0.1 eV and makes Pyr. I dislocation less stable.

Semi-circular dislocation bow out

In the current analytical model, we choose the dislocation bow-out model instead of the double-kink model because MD simulations show that the $\langle c + a \rangle$ dislocations glide readily on Pyramidal planes under conditions similar to Mg experiments at room temperature, i.e. under a resolved shear stress of less than 100 MPa at 300 K. Under these conditions, the glide mechanism does not involve the kink-pair behaviour of screw dislocations in bcc metals. We approximate the bow out geometry as circular arc with arc length s and area A given parametrically as

$$s = 2r \sin^{-1} \left(\frac{l}{2r} \right) \quad (3)$$

$$A = r^2 \sin^{-1} \left(\frac{l}{2r} \right) - \frac{rl}{2} \sqrt{1 - \left(\frac{l}{2r} \right)^2} \quad (4)$$

in terms of the equilibrium radius of curvature r of the arc that is determined by a balance between the resolved shear stress τ and the dislocation line tension T , $r = T/b\tau$.



```
../../../../pic/tex/sim_cell/sim_cell-crop.pdf
```

Fig. S 1. Schematic of the simulation cell used in the Nudged Elastic Band calculations. (a) $\langle c + a \rangle$ screw dislocation dissociated on the Pyramidal II plane. (b) $\langle c + a \rangle$ screw dislocation dissociated on the Pyr. I plane. Identical boundary conditions (atoms fixed according to the displacement field of a Volterra $\langle c + a \rangle$ dislocation plus any displacement corresponding to applied stresses) are used for all replicas of the calculations.

```
../../../../pic/py/gamma_iso/comb_all-crop.pdf
```

Fig. S 2. Generalized stacking fault energy surfaces of pyramidal I and II planes for hcp metals (a) Mg,²⁵ (b) Ti,⁷⁰ (c) Zr,⁷¹ (d) Co,⁷² (e) Cd⁷³ and (f) Zn⁷⁴ as calculated by various interatomic potentials. Positions (indicated by the “×” symbols) and energies of the metastable stacking faults are calculated under full atomic relaxation.

../../../../pic/py/combine_sxx_sxy_schem-crop.pdf

Fig. S 3. (a) Energy differences $E_I - E_{II}$ as a function of applied normal stress σ_{xx} . (b,c) Energy profiles on the minimum energy path for $\langle \mathbf{c} + \mathbf{a} \rangle$ screw dislocation cross-slip from Pyr. II to I planes calculated by NEB under applied normal stress σ_{xx} . (d) Energy differences $E_I - E_{II}$ as a function of applied normal stress σ_{xy} . (e,f) Energy profiles on the minimum energy path for $\langle \mathbf{c} + \mathbf{a} \rangle$ screw dislocation cross-slip from Pyr. II to I planes calculated by NEB under applied normal stress σ_{xy} . For $\sigma_{xy} = 250$ MPa, convergence is assumed when the maximum force on atoms is below $7 \times 10^{-3} \text{ eV}\text{\AA}^{-1}$. A metastable structure (MTS) is found at $\sigma_{xx} = 250$ MPa and $\sigma_{xy} = \pm 125$ MPa.